High-resolution simulations of unstable cylindrical gravity currents undergoing wandering and splitting motions in a rotating system

Albert Dai, and Ching-Sen Wu

Citation: Physics of Fluids **30**, 026601 (2018);
View online: https://doi.org/10.1063/1.5011070
View Table of Contents: http://aip.scitation.org/toc/phf/30/2
Published by the American Institute of Physics

High-resolution simulations of unstable cylindrical gravity currents undergoing wandering and splitting motions in a rotating system

Albert Dai[1,a)] and Ching-Sen Wu[2]
[1]*Department of Engineering Science and Ocean Engineering, National Taiwan University, Taipei, Taiwan*
[2]*Department of Civil Engineering, National Ilan University, Yilan, Taiwan*

(Received 30 October 2017; accepted 26 January 2018; published online 8 February 2018)

High-resolution simulations of *unstable* cylindrical gravity currents when wandering and splitting motions occur in a rotating system are reported. In this study, our attention is focused on the situation of *unstable* rotating cylindrical gravity currents when the ratio of Coriolis to inertia forces is larger, namely, $0.5 \leq C \leq 2.0$, in comparison to the *stable* ones when $C \leq 0.3$ as investigated previously by the authors. The simulations reproduce the major features of the *unstable* rotating cylindrical gravity currents observed in the laboratory, i.e., vortex-wandering or vortex-splitting following the contraction-relaxation motion, and good agreement is found when compared with the experimental results on the outrush radius of the advancing front and on the number of bulges. Furthermore, the simulations provide energy budget information which could not be attained in the laboratory. After the heavy fluid is released, the heavy fluid collapses and a contraction-relaxation motion is at work for approximately 2−3 revolutions of the system. During the contraction-relaxation motion of the heavy fluid, the *unstable* rotating cylindrical gravity currents behave similar to the *stable* ones. Towards the end of the contraction-relaxation motion, the dissipation rate in the system reaches a local minimum and a quasi-geostrophic equilibrium state is reached. After the quasi-geostrophic equilibrium state, vortex-wandering or vortex-splitting may occur depending on the ratio of Coriolis to inertia forces. The vortex-splitting process begins with non-axisymmetric bulges and, as the bulges grow, the kinetic energy increases at the expense of decreasing potential energy in the system. The completion of vortex-splitting is accompanied by a local maximum of dissipation rate and a local maximum of kinetic energy in the system. A striking feature of the *unstable* rotating cylindrical gravity currents is the persistent upwelling and downwelling motions, which are observed for both the vortex-wandering and vortex-splitting motions and were not previously documented for such flows. Depending on the Reynolds number, the bulges around the circumference of the *unstable* rotating cylindrical gravity currents may or may not develop into cutoff distinct circulations. The number of bulges is seen to be dependent on the ratio of Coriolis to inertia forces but independent of the Reynolds number for the range of Reynolds number considered in this study. *Published by AIP Publishing.* https://doi.org/10.1063/1.5011070

I. INTRODUCTION

Gravity currents, also known as buoyancy or density currents, are ubiquitous phenomena in natural and man-made environments when fluid of one density flows into fluid of a different density. The density difference between the fluids, which may be attributed to temperature differentials, dissolved materials, and suspended sediments, provides the driving force for such flows. The readers are referred to Refs. 1 and 2 for a comprehensive introduction to this topic and examples in geophysical and industrial environments.

Gravity currents have been studied extensively in the laboratory using lock-exchange experiments. In a typical lock-exchange experiment, a horizontal channel with a rectangular cross section is used and a vertical barrier is placed inside the channel, where the two sides of the barrier are filled with fluids of different densities. Removal of the barrier then sets the two fluids into motion. Gravity currents produced in the typical lock-exchange experiments propagate as statistically two-dimensional, planar gravity currents. Planar gravity currents have drawn the most attention and have been investigated with the help of laboratory experiments (e.g., Refs. 3–13) and numerical simulations (e.g., Refs. 14–19), to mention but a few. There are also situations when the gravity currents are not constrained by the lateral walls but are allowed to spread radially outward over the entire horizontal plane. In such situations, the gravity currents propagate as statistically axisymmetric flows, also known as cylindrical gravity currents. In contrast to the planar gravity currents, experimental and computational investigations of the cylindrical gravity currents are comparatively limited.[3,4,20–28]

In situations when the cylindrical gravity currents propagate in a rotating system, the influence of the Coriolis force may play a major role.[29–33] A related example in oceanography is the warm or cold core "ring," "vortex" or "lens,"[34–37] which is a flow structure associated with an isolated mass of anomalous water, significantly warmer or colder, saltier or fresher than its surroundings and it is not uncommon that such vortices can disintegrate into several pieces as discussed in Ref. 34.

a)hdai@ntu.edu.tw

Such flows under the influence of the Coriolis force are modeled in the laboratory by performing lock-exchange experiments for cylindrical gravity currents on a rotating turntable. For cylindrical gravity currents produced from a full-depth cylindrical lock-release in a rotating system, the governing parameter is the ratio of Coriolis to inertia forces, i.e.,

$$C = \frac{\tilde{\Omega}\tilde{R}_0}{\sqrt{\tilde{g}_0'\tilde{H}}}, \tag{1}$$

where $\tilde{\Omega}$ is the angular velocity of the rotating system, $\tilde{R}_0$ is the radius of the cylindrical lock, $\tilde{H}$ is the depth of the fluid, and $\tilde{g}_0'$ is the reduced gravity.

In the experiments of Ref. 34, the heavy fluid is confined inside the cylindrical lock, of which the depth is the same as that of the light ambient fluid, so the vortex is formed on the bottom once the lock is removed. It was reported that, when $C \leq 0.37$, the "bottom vortex" is stable in the sense that a state of equilibrium, i.e., a steady-state lens, is approached. Alternatively, when $C > 0.37$, the "bottom vortex" adjusts to a quasi-geostrophic equilibrium state but then becomes unstable in the sense that it may move around the centre of rotation, i.e., vortex-wandering, or may break up into multiple distinct circulations, i.e., vortex-splitting.

For *stable* cylindrical gravity currents in a rotating system, i.e., "bottom vortex" when $C \leq 0.37$, the problem using laboratory experiments, shallow-water formulation, and finite-difference numerical solutions of the axisymmetric Navier-Stokes equations was investigated in Refs. 38–40. Following the release of heavy fluid, Coriolis effects are negligible during the initial one-tenth of a revolution of the system and a maximum radius of propagation is reached in less than half of a revolution of the system. Thereafter a contraction-relaxation motion of the heavy fluid and a regular series of outwardly propagating new pulses were observed. The problem by means of three-dimensional high-resolution simulations of the Navier-Stokes equations and provided more in-depth flow information, including the energy budgets and lobe-and-cleft structure, during the adjustment process was investigated in Ref. 28.

For *unstable* cylindrical gravity currents in a rotating system, i.e., "bottom vortex" when $C > 0.37$, the "bottom vortex" initially adjusts to a quasi-geostrophic equilibrium state and, at this state, its radius is related to the ratio of Coriolis to inertia forces by

$$\frac{\tilde{R} - \tilde{R}_0}{\tilde{R}_0} \approx \frac{1}{2C}, \tag{2}$$

as confirmed by Ref. 34. After adjustment, the "bottom vortex" becomes unstable and exhibits non-axisymmetric bulges, which grow to an amplitude such that they become cutoff distinct circulations for sufficiently large ratio of Coriolis to inertia forces. The number of bulges, m, is related to the ratio of Coriolis to inertia forces by

$$m \approx 3.6C, \tag{3}$$

where m takes integer values only. Here $m = 1$ denotes the vortex-wandering motion and $m \geq 2$ denotes the vortex-splitting motion. It was also confirmed by Ref. 34 that the aspect ratio of the cylindrical lock, $\tilde{R}_0\tilde{H}^{-1}$, has unnoticed influence on the results. Experiments in which the fluid inside the cylindrical lock is less dense than the environment so the vortex is formed at the free surface, i.e., "surface vortex," rather than on the bottom were performed in Ref. 41. It was found that the "surface vortex" is always unstable, even when $C \leq 0.37$. The stability of the "bottom vortex" when $C \leq 0.37$ to the action of the viscous Ekman layer at the bottom was attributed in Ref. 41. The "surface vortex" by direct numerical simulation was investigated in Ref. 42 and good agreement with the experiments in Ref. 41 was found.

This study aims at deepening our understanding of the *unstable* rotating cylindrical gravity currents, i.e., the unstable "bottom vortex" when $C > 0.37$. In the laboratory, the rotating experiments can provide the number of bulges but there exist technical difficulties in obtaining the time evolution of the whole density and velocity fields, especially when vortex-wandering or vortex-splitting occurs. Due to the non-axisymmetric nature of the *unstable* rotating cylindrical gravity currents, the detailed flow information must be captured by means of three-dimensional high-resolution simulations without imposed axisymmetry conditions.

This study is also a continuation of the three-dimensional high-resolution simulations of cylindrical gravity currents in a rotating system reported by Ref. 28 but aims at investigating the problem in the parameter range of $0.5 \leq C \leq 2.0$, in comparison to the *stable* rotating cylindrical gravity currents in the parameter range of $0 \leq C \leq 0.3$ reported in Ref. 28. Specifically, $C = 0.5, 0.75, 1.0, 1.25, 1.5, 1.75, 2.0$ are considered in this study. The investigation is conducted by means of three-dimensional high-resolution simulations of the incompressible variable-density Navier-Stokes equations with the Coriolis term. With the detailed information in the flow field, qualitative and quantitative measures for the formation of *unstable* rotating cylindrical gravity currents are now shown more clearly for the first time. In Sec. II, we describe the formulation of the problem and the numerical procedure. The qualitative and quantitative results are presented in Sec. III. Finally, conclusions are drawn in Sec. IV.

II. FORMULATION

Figure 1 gives a sketch of the configuration for simulations of cylindrical gravity currents produced by a full-depth lock-release in a rotating system. The nomenclature follows Ref. 28 but for the reader's convenience, the formulation is presented here without being curtailed. The heavy fluid of density $\tilde{\rho}_1$ is confined in the cylindrical lock region of radius $\tilde{R}_0$ and filled to the same depth $\tilde{H}$ as the light ambient fluid outside the cylindrical lock region. The density of the light ambient fluid is $\tilde{\rho}_0$. Here the radius of the cylindrical lock is chosen the same as the depth of the fluid, i.e., $\tilde{R}_0 = \tilde{H}$. Before the release of heavy fluid, the system of heavy fluid and light ambient fluid is in solid-body rotation with constant angular velocity $\tilde{\Omega}$ about the vertical axis x_3 with a gravitational acceleration in the antiparallel direction of x_3. In tensor notation, the governing

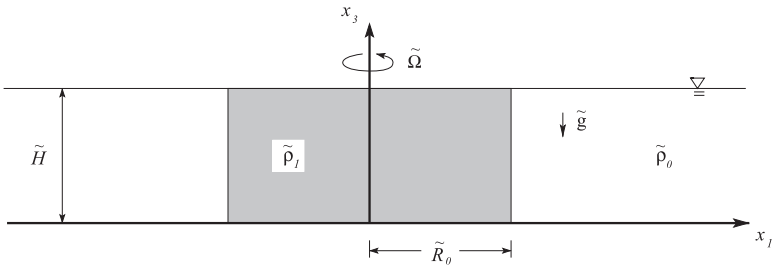

FIG. 1. Sketch of the initial condition for a cylindrical gravity current, produced by a full-depth lock release, in a rotating system. At $t = 0$, heavy fluid of density $\tilde{\rho}_1$ is confined in the cylindrical lock of which the radius is $\tilde{R}_0 = \tilde{H}$. Outside the cylindrical lock is the light ambient fluid of density $\tilde{\rho}_0$. Before the heavy fluid is released from the lock, the system is in solid-body rotation with constant angular velocity $\tilde{\Omega}$ about the vertical axis x_3. Removal of the cylindrical lock sets the quiescent fluid, observed in the rotating frame, into motion.

equations, with the Coriolis term and using the Boussinesq approximation, take the form

$$\frac{\partial u_k}{\partial x_k} = 0, \tag{4}$$

$$\frac{\partial u_i}{\partial t} + \frac{\partial (u_i u_k)}{\partial x_k} = \rho e_i^g - \frac{\partial p}{\partial x_i} - 2CR_0^{-1}\varepsilon_{ijk} e_j^{\Omega} u_k + \frac{1}{Re}\frac{\partial^2 u_i}{\partial x_k \partial x_k}, \tag{5}$$

$$\frac{\partial \rho}{\partial t} + \frac{\partial (\rho u_k)}{\partial x_k} = \frac{1}{ReSc}\frac{\partial^2 \rho}{\partial x_k \partial x_k}. \tag{6}$$

Here u_i denotes the velocity, ρ denotes the density, e_i^g denotes the unit vector in the direction of gravity, e_j^{Ω} denotes the unit vector in the direction of rotation, p denotes the pressure, and ε_{ijk} denotes the Levi-Civita symbol. Please note that the centrifugal term is combined with the pressure term in (5) without loss of generality. The set of Eqs. (4)–(6) has been made dimensionless by the lock height, $\tilde{H}$, as the length scale and the buoyancy velocity

$$\tilde{u}_b = \sqrt{\tilde{g}_0' \tilde{H}} \quad \text{with} \quad \tilde{g}_0' = \tilde{g}\frac{\tilde{\rho}_1 - \tilde{\rho}_0}{\tilde{\rho}_0}, \tag{7}$$

as the velocity scale. The lock height, $\tilde{H}$, is used as the length scale and the dimensionless radius of the lock is defined as $R_0 = \tilde{R}_0/\tilde{H}$. Since the radius of the cylindrical lock is set to be the same as the depth of the fluid, the dimensionless radius of the lock is unity, i.e., $R_0 = 1$. The dimensionless density, i.e., the concentration of fluid mixture, is given by

$$\rho = \frac{\tilde{\rho} - \tilde{\rho}_0}{\tilde{\rho}_1 - \tilde{\rho}_0}. \tag{8}$$

The relevant dimensionless parameters are the ratio of Coriolis to inertia forces, defined by (1) and the Reynolds number Re defined by

$$Re = \frac{\tilde{u}_b \tilde{H}}{\tilde{\nu}}. \tag{9}$$

The two fluids are assumed to have identical kinematic viscosities $\tilde{\nu}$ and diffusion coefficients $\tilde{\kappa}$. They are related by the Schmidt number

$$Sc = \frac{\tilde{\nu}}{\tilde{\kappa}}, \tag{10}$$

which represents the ratio of the kinematic viscosity to molecular diffusivity. In saline experiments, $Sc \approx 700$, but it has been observed by many researchers (e.g., Refs. 14, 15, 43, and 44) that the influence of Schmidt number on the dynamics of the gravity current is weak as long as $Sc \approx O(1)$ or larger. Here we follow suit and employ $Sc = 1$ in the simulations. The Ekman number, which expresses the ratio of viscous to Coriolis forces, can be expressed in terms of the previous dimensionless parameters by $E = R_0(CRe)^{-1}$.

The set of equations in the velocity-pressure formulation is solved with resolution $N_{x_1} \times N_{x_2} \times N_{x_3}$. The length is nondimensionalized by the lock height, $\tilde{H}$, and the flow domain is $L_{x_1} \times L_{x_2} \times L_{x_3} = 10 \times 10 \times 1$ to allow unhindered development of the currents. Fourier expansion with periodic boundary condition is employed in the horizontal directions, i.e., x_1 and x_2. Chebyshev expansion with Gauss-Lobatto quadrature points is employed in the wall-normal direction, i.e., x_3. As argued by Ref. 40, the free surface deviates from the horizontal but neglecting such a deviation is justified for small density contrast between heavy and light ambient fluids and for ratio of Coriolis to inertia forces of order unity. Following previous experimental and numerical investigations,[28,38,40] no-slip and no-stress conditions are employed for the velocity field at the bottom and top boundaries, respectively, and no-flux condition is employed for the density field at both the bottom and top boundaries. The influence of periodic boundary condition in the horizontal directions is considered unimportant here since previous investigations[14,45] have shown that the interaction of the gravity currents with the boundary becomes important only when the front reaches within one depth scale of the boundary for the planar case and even less significant for the cylindrical case. As will be shown later, the maximum outrush radius in this study $R \approx 2.2$ occurs when $C = 0.5$ and our computational domain is sufficiently large to avoid the influence of the boundary.

The flow field is advanced in time by the low-storage third-order Runge-Kutta scheme.[46] The convection, buoyancy, and Coriolis terms are treated explicitly while the diffusion terms are treated implicitly with the Crank-Nicolson scheme. The convection term is evaluated using the Arakawa method[47] to reduce the aliasing error. The de-aliased pseudospectral code has been employed in Ref. 28 for the investigation of cylindrical gravity currents in a rotating system and good agreement with experimental and theoretical results was found. In all simulations, the velocity field was initialized with quiescent conditions everywhere. The initial density field is prescribed unity in the heavy fluid region and zero elsewhere with a smooth error-function type transition in the interface region.[48] To resolve the flow structures of the gravity currents in the flow domain, adequate resolution requires a grid size of $\Delta x_1 \approx (ReSc)^{-1/2}$ in the horizontal directions.[14] In this work, five different Reynolds numbers are considered: $Re = 500$, 1000, 2000, 4000, and 6000. The grid employed for $Re = 500$ and

1000 is $N_{x_1} \times N_{x_2} \times N_{x_3} = 256 \times 256 \times 84$, the grid for $Re = 2000$ and 4000 is $512 \times 512 \times 128$, and the grid for $Re = 6000$ is $616 \times 616 \times 160$ and thus the grids involve 5.5, 33.6, and 60.7×10^6 grid points, respectively. The time step was chosen to produce a Courant number less than 0.5. The Courant number, which is checked at very grid point and during the entire simulation time, is defined as the summation in all three directions of flow velocity multiplied by the time step and divided by the grid size.

III. RESULTS

A. Vortex-wandering motion, i.e., $m = 1$

We begin by presenting the results for the cylindrical gravity current, produced by a full-depth lock release, in a rotating system at $C = 0.5$ and $Re = 4000$. It is worth noting that this ratio of Coriolis to inertia forces $C = 0.5$ marginally exceeds the limit for stability and this case serves as a bridge between the *stable* currents reported by Ref. 28 and the *unstable* ones with vortex-splitting, i.e., $m \geq 2$. As will be shown in more detail below, the current at $C = 0.5$ exhibits the contraction-relaxation motion, similar to the *stable* currents, prior to the quasi-geostrophic equilibrium state and displays a non-axisymmetric vortex-wandering motion, i.e., $m = 1$, after the quasi-geostrophic equilibrium state.

The initial configuration of the problem considered in this study is sketched in Fig. 1. Before the lock is removed, the system is in solid-body rotation and both heavy and light fluids are quiescent in the rotating frame of reference. After the lock is removed, a current propagating radially outward on the bottom boundary is produced. It is well known from previous investigations (e.g., Refs. 28, 38, and 40) that the *stable* currents have features without counterparts in non-rotating situations. A major feature in the *stable* currents, due to the presence of the Coriolis force, is the attainment of a maximum radius of propagation.

Figure 2 shows one quarter of the current at $C = 0.5$ and $Re = 4000$ visualized by a density isosurface of $\rho = 0.15$. For illustrative purposes, the time instances are chosen at $\Omega t/2\pi = 1.0$, 3.0, i.e., when the system has rotated through 1.0 and 3.0 revolutions. As the *stable* currents do during the adjustment to an equilibrium state of motion, the *unstable* current at $C = 0.5$ and $Re = 4000$ exhibits the contraction-relaxation motion between the centre and the outer rim of the heavy fluid prior to $\Omega t/2\pi \approx 2.5$. Also, the core region of heavy fluid at the centre of rotation remains in contact with the surface, as confirmed by the observations for the currents produced from a full-depth lock release in the laboratory.[34,49]

We may also visualize the currents using quantities averaged in the wall-normal and in the azimuthal directions. For any flow variable f, its average in the wall-normal direction is

$$\hat{f}(x_1, x_2) = \int_0^1 f(x_1, x_2, x_3)\, dx_3, \tag{11}$$

and its average in the azimuthal direction is

$$\bar{f}(r, x_3) = \frac{1}{2\pi} \int_0^{2\pi} f(r, \theta, x_3)\, d\theta, \tag{12}$$

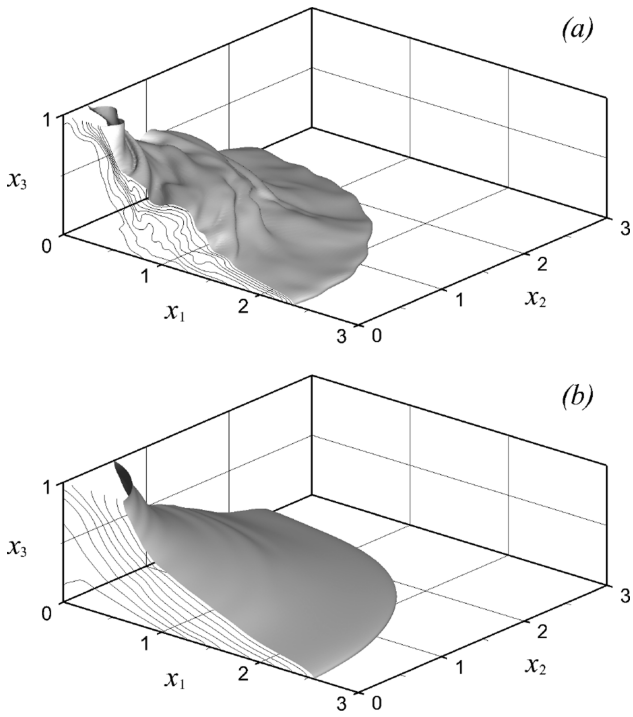

FIG. 2. Rotating cylindrical gravity current at $C = 0.5$ and $Re = 4000$ visualized in one quadrant of the computational domain by isosurface of $\rho = 0.15$. For illustrative purposes, time instances are chosen at $\Omega t/2\pi = 1.0$ (a), 3.0 (b). Density contours are also shown by solid lines in the (x_1, x_3) plane.

where (r, θ, x_3) is converted from (x_1, x_2, x_3), in a consistent way as the velocity in cylindrical coordinates (u_r, u_θ, u_3) is converted from that in Cartesian coordinates (u_1, u_2, u_3).

Figure 3 shows the density averaged in the wall-normal direction. It is observed that, prior to $\Omega t/2\pi \approx 0.2$, the current maintains nearly perfect axisymmetry, as also confirmed in Ref. 28 for the *stable* currents. Afterwards, the variations in the azimuthal direction develop and the flow becomes three-dimensional, as shown in Fig. 3 at $\Omega t/2\pi = 0.3$, 0.5. During the initial period of time of approximately 2.5 revolutions of the system, the current exhibits contraction-relaxation motion. The contraction-relaxation motion gradually diminishes as the system approaches the quasi-geostrophic equilibrium state.

To better visualize the contraction-relaxation motion of the heavy fluid and the new pulses travelling from near the centre of rotation to the outer rim of the heavy fluid, Fig. 4 shows the density and velocity averaged in the azimuthal direction at different time instances in the range of $0.8 \leq \Omega t/2\pi \leq 1.4$ for the current at $C = 0.5$ and $Re = 4000$. As shown in Fig. 4(a) at $\Omega t/2\pi = 0.8$, the body of the current contracts radially inward and the contracting fluid meets outward propagating fluid. The dashed boxes indicate the region where inward and outward moving fluids meet, and a new pulse begins to emerge in the upper part of the body of the current. At $\Omega t/2\pi = 1.0$, 1.2 shown in Figs. 4(b) and 4(c), the region where inward and outward moving fluids meet, as indicated by the dashed box, continues to move outward. At $\Omega t/2\pi = 1.4$ shown in Fig. 4(d), a new pulse begins to form and the contraction-relaxation motion repeats itself. The contraction-relaxation motion and the new pulses for the current at $C = 0.5$ and $Re = 4000$ prior to

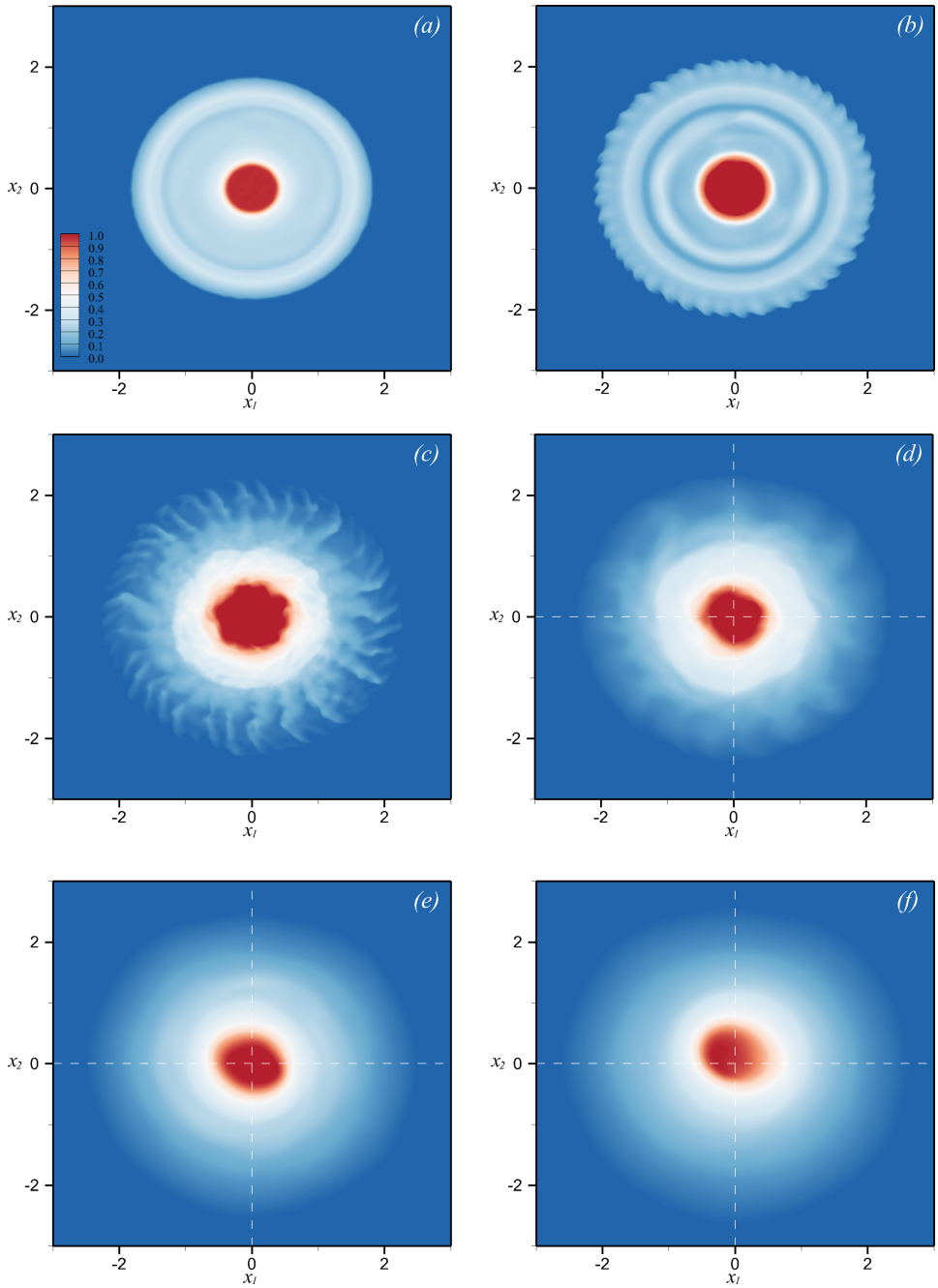

FIG. 3. Rotating cylindrical gravity current at $C = 0.5$ and $Re = 4000$ visualized by the density averaged in the wall-normal direction, i.e., $\hat{\rho}(x_1, x_2)$, plotted on the (x_1, x_2) plane. For illustrative purposes, time instances are chosen at $\Omega t/2\pi = 0.2$ (a), 0.3 (b), 0.5 (c), 1.0 (d), 2.0 (e), 3.0 (f). The white dashed lines in (d)–(f) represent $x_1 = 0$ and $x_2 = 0$ and serve as a guide to show the wandering motion more clearly.

$\Omega t/2\pi \approx 2.5$ are consistent with the observations for the *stable* currents at $C \leq 0.37$ made in Ref. 28, to which the readers are referred for more detailed analyses of the rearrangement of the heavy fluid in the contraction-relaxation motion. Please note that although the contraction-relaxation motion prior to $\Omega t/2\pi \approx 2.5$ is consistent with previous investigations by Refs. 40 and 28 for the *stable* currents, the radius of the current in this study is shorter and as such the new pulse formation is less clearly seen in Fig. 4 than in the energy budget analysis, which will be discussed later and in which the energy is transformed between potential energy and kinetic energy.

After $\Omega t/2\pi \approx 2.5$, the core of the current begins to move around the centre of rotation in the cyclonic direction, which we term vortex-wandering, as shown in Fig. 3 at $\Omega t/2\pi = 3.0$. A striking feature of the *unstable* current, when vortex-wandering occurs, is the presence of upwelling and downwelling motions around the core region of *unstable* current. Figure 5 shows the density and velocity contours taken at different levels for the *unstable* current at $C = 0.5$ and $Re = 4000$ and, for illustrative purposes, the time instance is chosen at $\Omega t/2\pi = 3.0$, when vortex-wandering occurs. While the vectors in Fig. 5 represent the velocity field in the x_1-x_2 plane, the solid (dashed) lines represent the contours of positive (negative) values of the vertical velocity u_3. It becomes clear that the upwelling and downwelling motions manifest themselves across the depth of the flow from the bottom to the top boundary. The centre of upwelling motion and the centre of downwelling motion rotate around each other in the cyclonic direction and move along with the wandering vortex. It is important to note that such upwelling and downwelling

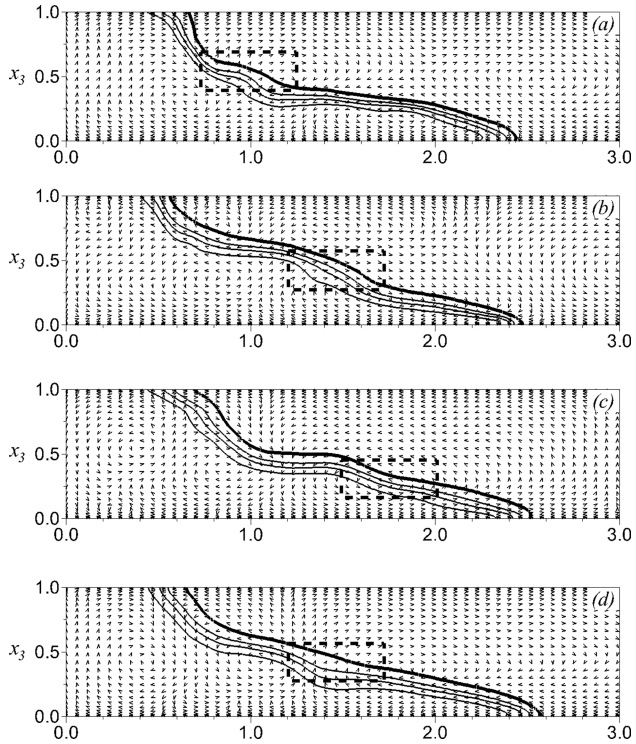

FIG. 4. Rotating cylindrical gravity current at $C = 0.5$ and $Re = 4000$ visualized by the density and velocity averaged in the azimuthal direction, i.e., $\bar{\rho}(r, x_3)$, $\bar{u}_r(r, x_3)$ and $\bar{u}_3(r, x_3)$, plotted on the (r, x_3) plane. For illustrative purposes, time instances are chosen at $\Omega t/2\pi = 0.8, 1.0, 1.2, 1.4$. Density contours are shown by the solid lines and velocity is shown by the vector field on the (r, x_3) plane. The dashed boxes indicate the regions where the contracting fluid meets outward propagating fluid and inside where a new pulse emerges.

motions are not present for the *stable* currents in the steady-state lens motion and were not documented in the literature for the *unstable* currents, either.

B. Vortex-splitting motion, i.e., $m \geq 2$

We now turn the attention to the rotating cylindrical gravity currents, produced by a full-depth lock release, when the ratio of Coriolis to inertia forces takes larger values of $C = 0.75, 1.0, 1.25, 1.5, 1.75, 2.0$ and the Reynolds number is chosen at $Re = 4000$. Under these conditions, the *unstable* currents exhibit the contraction-relaxation motion similar to the current at $C = 0.5$ and $Re = 4000$, prior to the quasi-geotrophic equilibrium state. However, after the quasi-geostrophic equilibrium state, instead of vortex-wandering, vortex-splitting occurs for the *unstable* currents at $0.75 \leq C \leq 2.0$ and $Re = 4000$. Such a special feature, namely, vortex-splitting, is distinct from vortex-wandering in the rotating cylindrical gravity current at $C = 0.5$ and $Re = 4000$. Since the vortex-splitting processes in the currents at $0.75 \leq C \leq 2.0$ and $Re = 4000$ are qualitatively similar, we present the detailed analysis for the case of $C = 1.0$ and $Re = 4000$ and the details for other cases are omitted for brevity.

As an example, Fig. 6 shows one quarter of the current at $C = 1.0$ and $Re = 4000$ visualized by a density isosurface of $\rho = 0.15$ and the time instances are chosen at $\Omega t/2\pi = 1.0, 5.0$. Prior to $\Omega t/2\pi \approx 2.2$, the *unstable* current is still in the adjustment towards the quasi-geotrophic equilibrium state and the contraction-relaxation motion is at work, as shown in Fig. 6(a); when vortex-splitting is completed, a distinct circulation is shown in the domain of Fig. 6(b).

Figure 7 shows the density averaged in the wall-normal direction for the current at $C = 1.0$ and $Re = 4000$ and the time instances are chosen at $\Omega t/2\pi = 0.5, 1.0, 2.0, 2.0, 4.0, 5.0$. During the vortex-splitting process, as shown in Fig. 7 for $\Omega t/2\pi \geq 3.0$, a number of bulges develop along the circumference of the current. These bulges grow in size as time progresses and eventually break up into several distinct circulations. Figure 8 shows the density and velocity contours taken at different levels for the *unstable* current at $C = 1.0$ and $Re = 4000$ and the time instance is chosen at $\Omega t/2\pi = 4.0$, when vortex-splitting occurs. Such detailed flow information during vortex-splitting shows that, as the bulges develop, upwelling and downwelling motions develop and pierce through the current.

C. Outrush radius and number of bulges

As the wandering and splitting motions have been presented in detail in Secs. III A and III B, here we compile the outrush radius of the currents and the number of bulges along the circumference of the currents at different values of the ratio of Coriolis to inertia forces while the Reynolds number is fixed at $Re = 4000$. We also compare our simulations with existing experimental and theoretical results.

The outrush radius is defined with the help of the density averaged in the wall-normal direction (e.g., Figs. 3 and 7) and is taken as the furthest radial position where heavy fluid reaches at the quasi-geostrophic equilibrium state. As will be shown later in Sec. III D, at the quasi-geostrophic equilibrium state, the contraction-relaxation motion diminishes and the potential energy and kinematic energy reach a temporarily stable state. Figure 9 shows the relationship between the outrush radius of the advancing front, at the quasi-geostrophic equilibrium state, and the ratio of Coriolis to inertia forces, which agrees well with the experiments and the theoretical relationship (2).

The number of bulges developing during vortex-splitting is found to depend on the ratio of Coriolis to inertia forces, as shown in Fig. 10 and described in (3). It is seen that the simulation results agree reasonably well with the experiments when $C > 1$ and agree remarkably well when $C \lesssim 1$.

D. Energy budgets

As elucidated by the energy budget analysis reported by Ref. 28 for the *stable* currents, during the contraction-relaxation motion of the heavy fluid, energy is transformed between potential energy and kinetic energy, while it is mainly the kinetic energy that is consumed by the dissipation. Here we perform the energy budget analysis for the *unstable* currents and our attention is particularly focused on the time after the quasi-geostrophic equilibrium state. Information on the energy budget can be difficult to attain in the experiments on a rotating turntable. Thanks to the three-dimensional high-resolution simulations, a complete and time-dependent energy budget is now made possible. In the following, we will provide a computational analysis of the energy budget for the *unstable* currents.

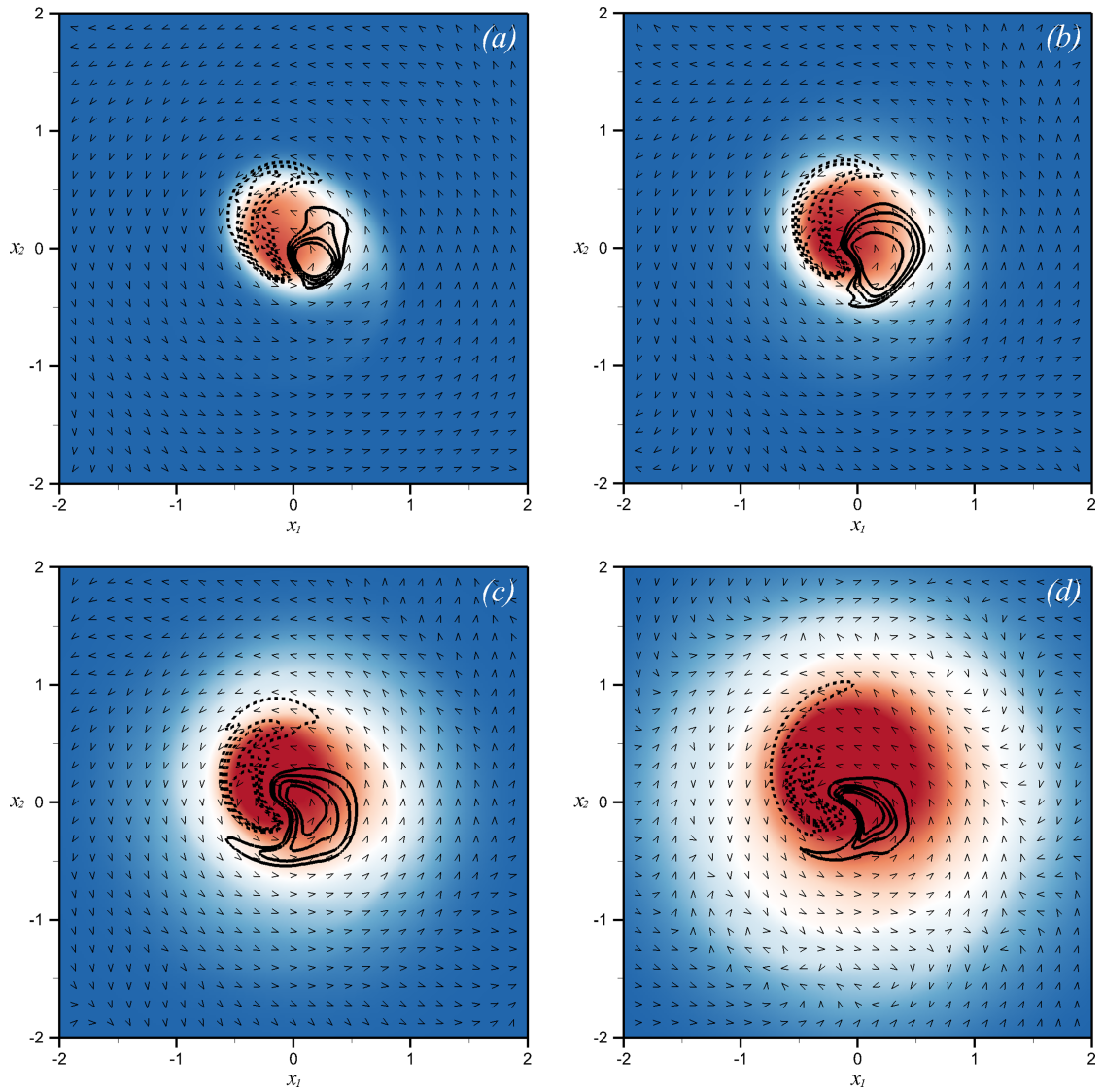

FIG. 5. Rotating cylindrical gravity current at $C = 0.5$, $Re = 4000$ and the time instance is chosen at $\Omega t/2\pi = 3.0$, when vortex-wandering, i.e., $m = 1$, occurs. For illustrative purposes, the horizontal velocity (shown by vectors), vertical velocity contours (shown by solid and dashed lines for positive and negative values of u_3), and density contours (shown in background with the same color range as Fig. 3) are selected at a number of x_1-x_2 planes, i.e., $x_3 = 0.785$ (a), 0.604 (b), 0.408 (c), 0.225 (d).

The equation for the time derivative of the kinetic energy is obtained by multiplying the momentum equation (5) by u_i, i.e.,

$$\frac{D}{Dt}\left(\frac{1}{2}u_i u_i\right) = -\frac{\partial}{\partial x_i}(pu_i) + \frac{2}{Re}\frac{\partial}{\partial x_j}\left(s_{ij}u_i\right) - \frac{2}{Re}s_{ij}s_{ij} - \rho u_3, \tag{13}$$

where D/Dt denotes the material derivative, s_{ij} denotes the strain rate tensor, $s_{ij} = \frac{1}{2}(u_{i,j} + u_{j,i})$, and u_3 denotes the velocity component in x_3 direction. It is interesting to note that the Coriolis term in (5) vanishes when multiplied by u_i and therefore the energy equation (13) has the same form as that for gravity currents in a non-rotating system. Integration of (13) over the entire flow domain $\mathscr{V}$ leads to the evolution equation of the total kinetic energy E_k, i.e.,

$$\frac{dE_k}{dt} = -\frac{2}{Re}\int_{\mathscr{V}} s_{ij}s_{ij}dV - \int_{\mathscr{V}}\rho u_3 dV, \quad E_k(t) = \int_{\mathscr{V}}\frac{1}{2}u_i u_i dV, \tag{14}$$

where the divergence terms on the right-hand side of (13) vanish after integration. We define the potential energy in the system as

$$E_p(t) = \int_{\mathscr{V}}\rho x_3 dV, \tag{15}$$

and the time derivative of the potential energy in the system is

$$\frac{dE_p}{dt} = \Phi_z + \Phi_i, \quad \Phi_z = \int_{\mathscr{V}} \rho u_3 dV, \quad \Phi_i = \int_{\mathscr{V}} x_3 \frac{D\rho}{Dt} dV, \tag{16}$$

where Φ_z represents the vertical buoyancy flux and Φ_i represents the rate of conversion from internal to potential energy due to irreversible diffusion in the density field.[50–52] We further define the irreversible conversion of internal energy into potential energy as

$$E_i = \int_0^t \Phi_i(\tau) d\tau. \tag{17}$$

The first term on the right-hand side of (14) represents the dissipation rate and we use E_d to denote the time integral of dissipation rate, i.e.,

$$E_d(t) = \int_0^t \epsilon(\tau) d\tau, \quad \epsilon = \frac{2}{Re} \int_{\mathscr{V}} s_{ij} s_{ij} dV. \tag{18}$$

Using (16)–(18), Eq. (14) is essentially a statement of energy balance, i.e., that $E_k + E_p + E_d - E_i$ is a constant during the motion of currents. Here the irreversible conversion of internal to potential energy, E_i, deserves some discussion. When the diffusion of density is absent, the potential energy in the system can only change via vertical buoyancy flux. With the diffusion of density, the potential energy can increase via irreversible diffusion of density even when the stratified fluid is quiescent. It was previously reported by Ref. 28 that the effects of diffusion in the density field on the potential energy can be neglected for the *stable* currents and the overall energy is conserved to a high degree of accuracy during the contraction-relaxation motion of the heavy fluid. We will show later in this section that while the effects of diffusion in the density field can be neglected during the contraction-relaxation motion of the heavy fluid prior to the quasi-geostrophic equilibrium state, the effects of diffusion in the density field may become significant during vortex-splitting after the quasi-geostrophic equilibrium state.

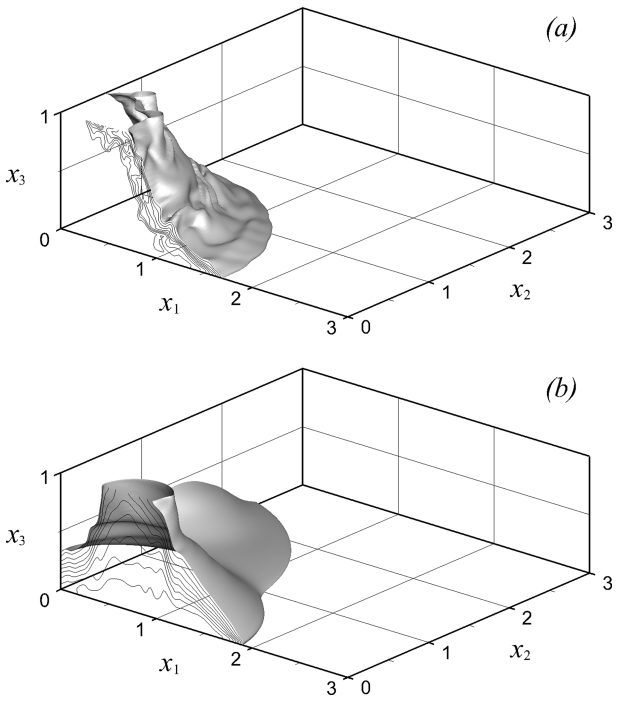

FIG. 6. Rotating cylindrical gravity current at $C = 1.0$ and $Re = 4000$ visualized in one quadrant of the computational domain by isosurface of $\rho = 0.15$. For illustrative purposes, time instances are chosen at $\Omega t/2\pi = 1.0$ (a), 5.0 (b). Density contours are also shown by solid lines in the (x_1, x_3) plane.

In order to quantitatively measure the upwelling and downwelling motions in the *unstable* rotating cylindrical gravity currents, the vertical buoyancy flux Φ_z can be further decomposed into two parts, i.e.,

$$\Phi_z = \Phi_z^+ + \Phi_z^-, \tag{19}$$

where

$$\Phi_z^+ = \int_{\mathscr{V}} \rho u_3|_{u_3>0} dV, \quad \Phi_z^- = \int_{\mathscr{V}} \rho u_3|_{u_3<0} dV, \tag{20}$$

are the vertical buoyancy fluxes associated with the upwelling motion and the downwelling motion, respectively.

Since the energy budgets for the *unstable* currents with $m \geq 2$ are qualitatively similar, we focus on the case of the current at $C = 1.0$ and $Re = 4000$ and other cases are not discussed in detail for brevity. The energy budgets are normalized with the initial potential energy in the system and the superscript "n" denotes normalized contributions. Figure 11 shows the energy budget analysis for the current at $C = 1.0$ and $Re = 4000$ prior to and after the quasi-geostrophic equilibrium state. In this case, the quasi-geostrophic equilibrium state is reached approximately when $\Omega t/2\pi \approx 2.2$. The overall energy in the system during the simulations, including the contribution from the term E_i^n, is observed to be conserved to a very high degree of accuracy.

Prior to the quasi-geostrophic equilibrium state, the heavy fluid initially collapses radially outward after being released and the kinetic energy increases at the expense of decreasing potential energy, as shown in Fig. 11(a). Following the collapse of heavy fluid, the contraction-relaxation motion of the heavy fluid is at work and both the potential energy and kinetic energy in the system show cyclic rise and fall until the quasi-geostrophic equilibrium state is approached. Figure 11(b) shows the time histories of the normalized dissipation rate, $\epsilon^n = dE_d^n/dt$, and the normalized rate of conversion of internal energy into potential energy, $\Phi_i^n = dE_i^n/dt$. It is observed that the first local maximum of dissipation rate occurs at $\Omega t/2\pi \approx 0.4$, which is approximately when the axisymmetric flow structures break up into three-dimensional ones as evidenced by the lobes developing on the outer rim of the current in Fig. 7(a).

When the quasi-geostrophic equilibrium state is approached, the potential energy in the system retains approximately $E_p^n \approx 0.7$ of the initial potential energy and the kinetic energy

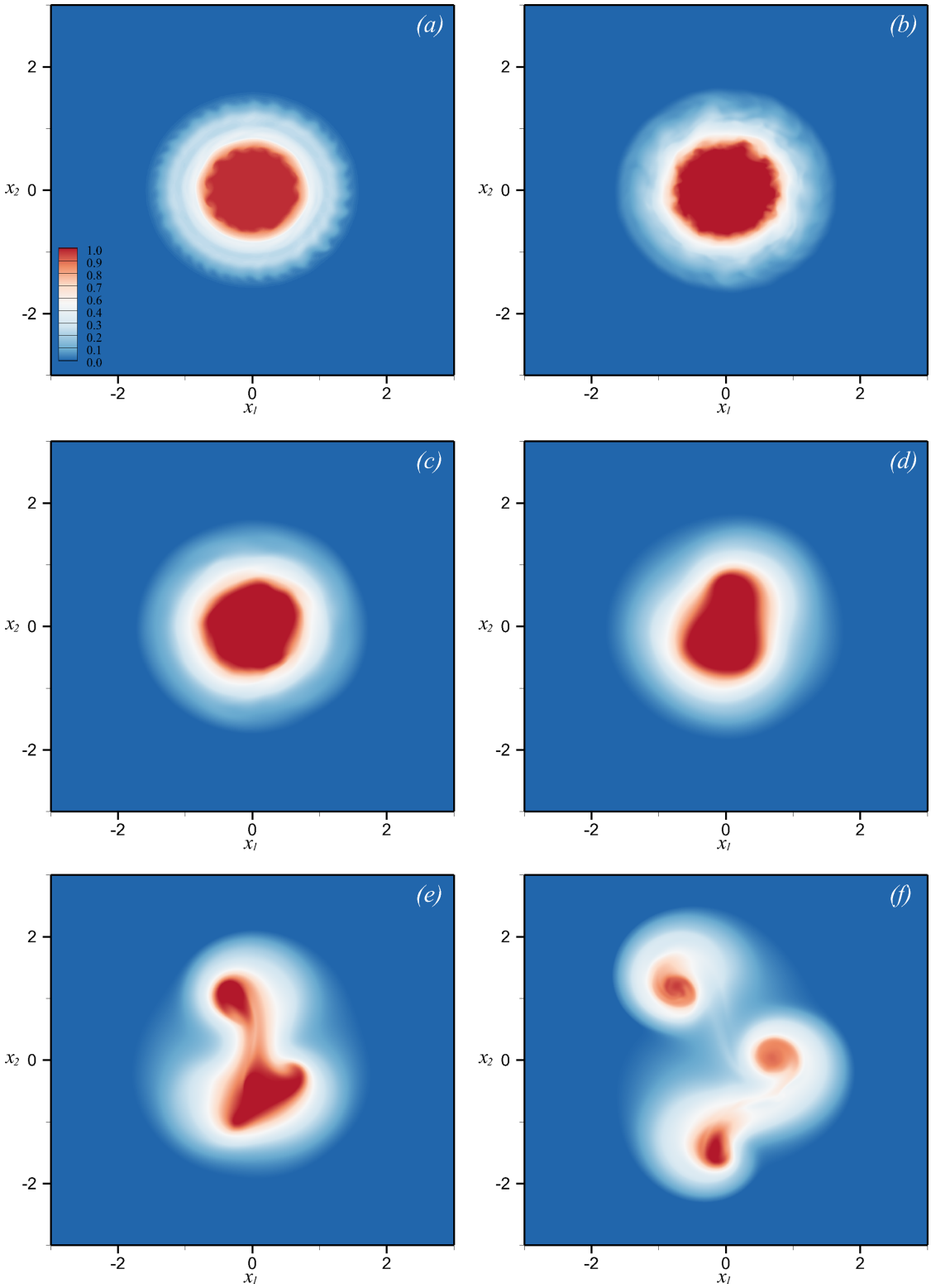

FIG. 7. Rotating cylindrical gravity current at $C = 1.0$ and $Re = 4000$ visualized by the density averaged in the wall-normal direction, i.e., $\hat{\rho}(x_1, x_2)$, plotted on the (x_1, x_2) plane. For illustrative purposes, time instances are chosen at $\Omega t/2\pi = 0.5$ (a), 1.0 (b), 2.0 (c), 3.0 (d), 4.0 (e), 5.0 (f).

remains approximately at $E_k^n \approx 0.1$. Based on the energy budgets at different values of C (not shown here), the fraction of initial potential energy that is retained at the quasi-geostrophic equilibrium state increases as the ratio of Coriolis to inertia forces increases. In addition, the dissipation rate decreases to a local minimum while the rate of conversion of internal energy into potential energy reaches a plateau value at $\Phi_i^n \approx 1.1\times10^{-3}$ as the quasi-geostrophic equilibrium state is approached. We should point out that, prior to the quasi-geostrophic equilibrium state, the conversion of internal energy into potential energy is comparatively small, i.e., $E_i^n < 2\%$. Therefore, it is not unreasonable to assume that the effects of diffusion in

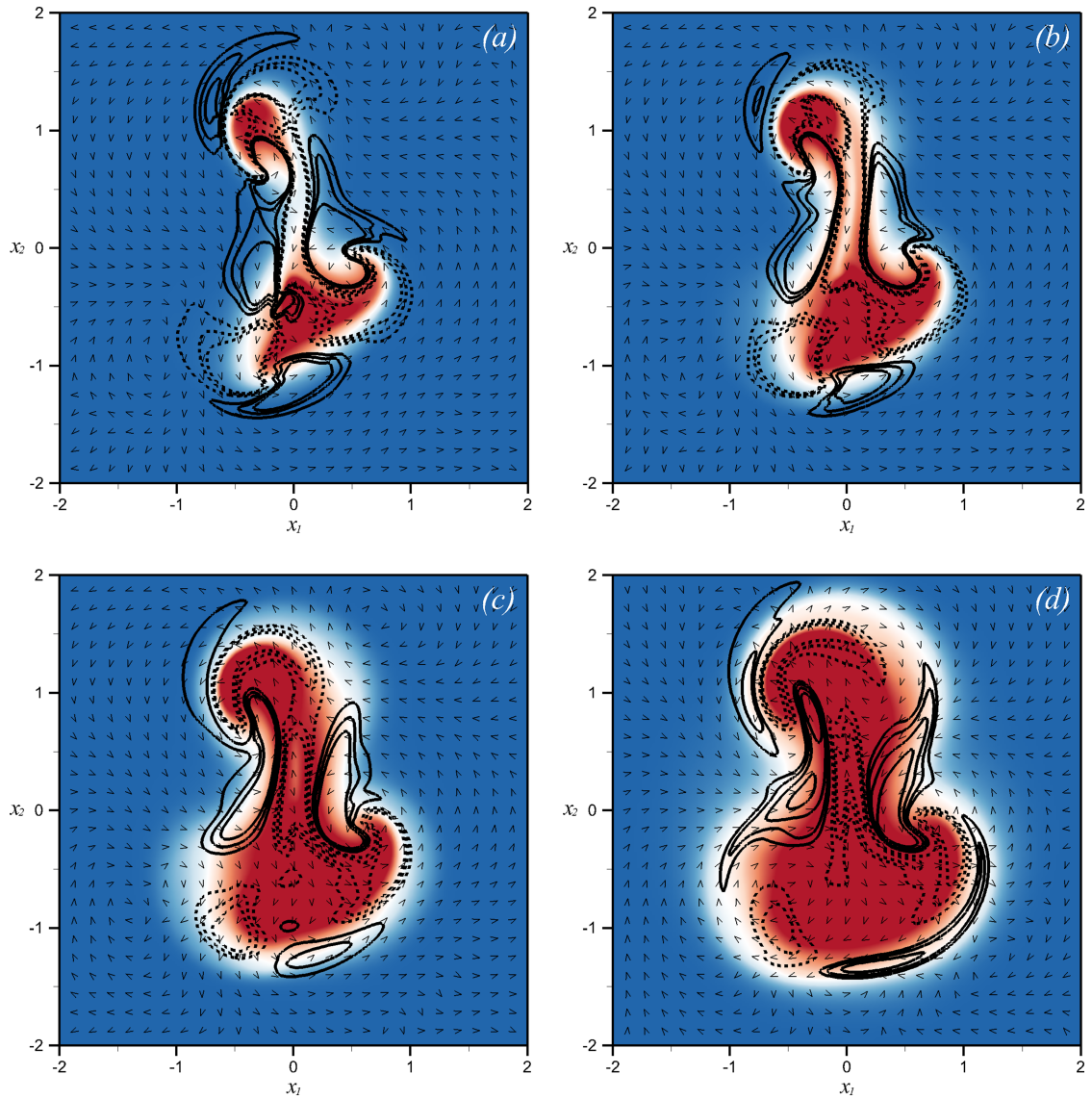

FIG. 8. Rotating cylindrical gravity current at $C = 1.0$, $Re = 4000$ and at $\Omega t/2\pi = 4.0$, when vortex-splitting, i.e., $m = 3$, occurs. For illustrative purposes, the horizontal velocity (shown by vectors), vertical velocity contours (shown by solid and dashed lines for positive and negative values of u_3), and density contours (shown in background with the same color range as Fig. 7) are selected at a number of x_1-x_2 planes, i.e., $x_3 = 0.785$ (a), 0.604 (b), 0.408 (c), 0.225 (d).

the density field on the potential energy are negligible during the adjustment prior to the quasi-geostrophic equilibrium state, as was done for the investigation of *stable* currents. Since the contraction-relaxation motion and the energy transformation between potential energy and kinetic energy in the system have been discussed in-depth in Ref. 28, we shall not further discuss the energy budgets prior to the quasi-geostrophic equilibrium state and we now turn the attention to the energy budgets after the quasi-geostrophic equilibrium state.

Please note that here we use vortex-splitting as a notion of "process" during which unstable disturbances grow and, as will be shown later, upward and downward fluxes increases, and finally distinct circulations emerge. When the vortex-splitting process occurs, Fig. 11(a) shows that the kinetic energy in the system increases significantly during $2.7 \lesssim \Omega t/2\pi \lesssim 5.7$ at the expense of decreasing potential energy. Such an observation confirms that in this study, the potential energy is the source for the kinetic energy of non-axisymmetric disturbances via baroclinic instability. As vortex-splitting occurs, Fig. 11(b) shows that the dissipation rate reaches a second local maximum and the rate of conversion of internal energy into potential energy also increases significantly. After vortex-splitting, the potential energy in the system maintains at a relatively constant level while the kinetic energy in the system decreases over time due to dissipation. It is worth noting that while it is appropriate to assume that the effects of diffusion in the density field on the potential energy are negligible prior to the quasi-geostrophic equilibrium state, it may not be so after the quasi-geostrophic equilibrium state, as an example, $E_i^n \approx 0.1$ at $\Omega t/2\pi = 10$.

A distinct feature arising in the *unstable* currents is the presence of upwelling and downwelling motions, as qualitatively described in Secs. III A–III C. Figure 11(c) shows quantitatively the upward buoyancy flux associated with upwelling

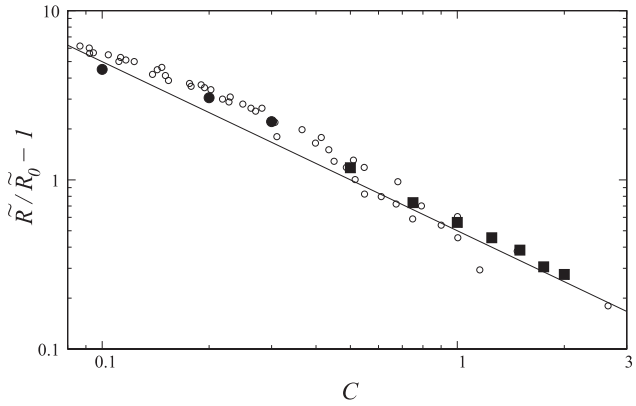

FIG. 9. Outrush radius of the advancing front, when the rotating cylindrical gravity current reaches the quasi-geostrophic equilibrium state, as a function of the ratio of Coriolis to inertia forces. The outrush radius is normalized by the radius of the cylindrical lock, i.e., $(\tilde{R} - \tilde{R}_0)/\tilde{R}_0$. Reynolds number is chosen at $Re = 4000$ in the simulations and at $Re \approx O(10^4)$ in the experiments of Ref. 34. Simulation results, including the *stable* rotating cylindrical gravity currents (•) for $C = 0.1, 0.2, 0.3$[28] and the data (■) from the present study, are compared with the experimental data (○) of Ref. 34 and with the theoretical relationship (2), represented by the straight solid line.

motion, the downward buoyancy flux associated with downwelling motion and the total vertical buoyancy flux. It is clear from the inset of Fig. 11(c) that the vortex-splitting process is accompanied by the increasing upward and downward buoyancy fluxes. Once vortex-splitting succeeds, the upwelling and downwelling motions recede after $\Omega t/2\pi \approx 4.3$ but nonzero upward and downward buoyancy fluxes remain.

E. Influence of the Reynolds number

The motion of the *unstable* currents can be expected to vary with the Reynolds number, due to the changing balance between the inertial and viscous forces. Here we examine

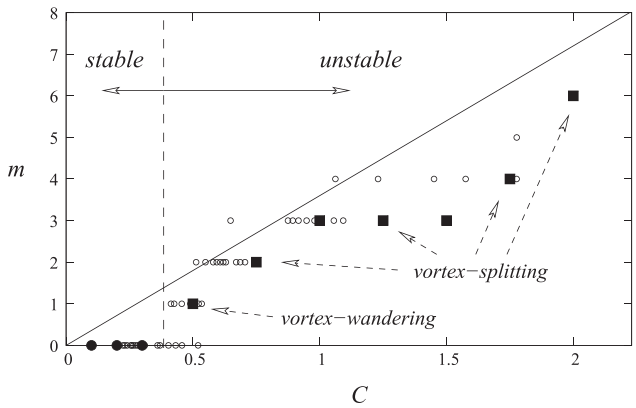

FIG. 10. Number of bulges along the circumference of the rotating cylindrical gravity currents, when vortex-slitting occurs, as a function of the ratio of Coriolis to inertia forces. Reynolds number is chosen at $Re = 4000$ in the simulations and at $Re \approx O(10^4)$ in the experiments of Ref. 34. Simulation results, including the *stable* rotating cylindrical gravity currents (•) for $C = 0.1, 0.2, 0.3$,[28] represented by $m = 0$, and the data (■) from the present study, are compared with the experimental data (○) of Ref. 34 and with the theoretical relationship (3), represented by the straight solid line. The vertical dashed line represents $C = 0.37$, which is a borderline between stable and unstable currents.

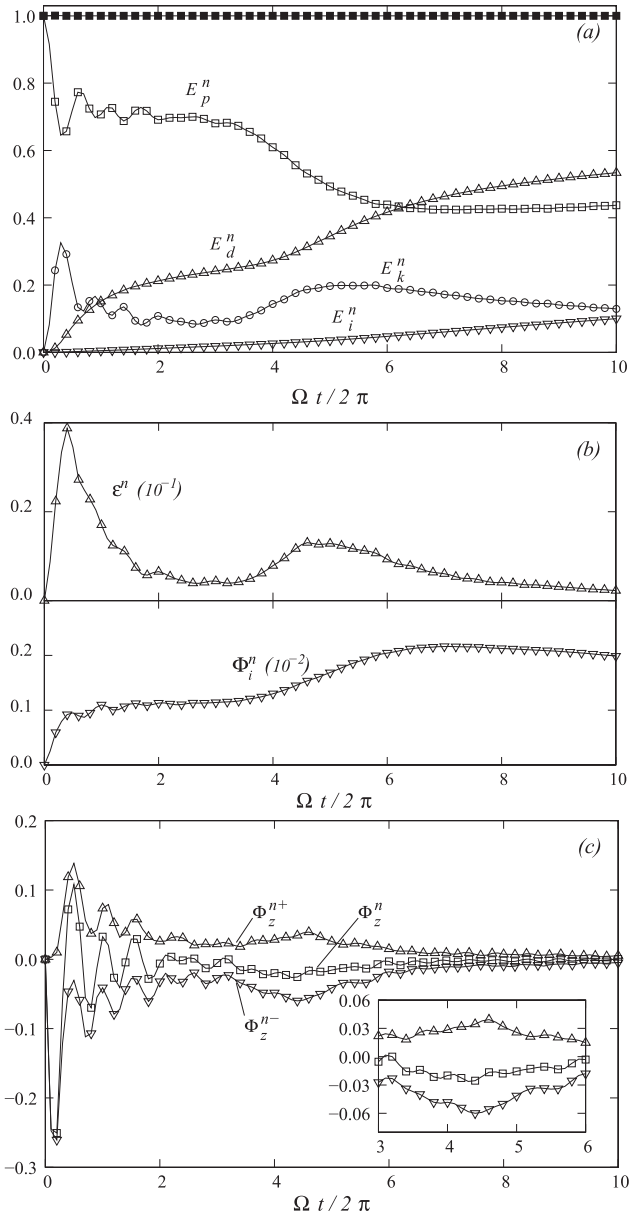

FIG. 11. Energy budget analysis for the rotating cylindrical gravity current at $C = 1.0$ and $Re = 4000$. Time is shown in terms of the number of revolutions that the system has rotated through, i.e., $\Omega t/2\pi$. Panel (a) shows the normalized potential energy E_p^n (□), kinetic energy E_k^n(○), dissipated energy E_d^n(△), conversion of internal energy into potential energy E_i^n(▽), and $E_k^n + E_p^n + E_d^n - E_i^n$(■). Panel (b) shows the normalized rate of dissipation $\epsilon^n = dE_d^n/dt$(△) and rate of conversion of internal energy into potential energy $\Phi_i^n = dE_i^n/dt$(▽). Panel (c) shows the normalized vertical buoyancy flux associated with upwelling motion Φ_z^{n+}(△), the vertical buoyancy flux associated with downwelling motion Φ_z^{n-}(▽), and the total buoyancy flux $\Phi_z^n = \Phi_z^{n+} + \Phi_z^{n-}$ (□). The inset in panel (c) shows the close-up view of the normalized buoyancy fluxes during $3 \le \Omega t/2\pi \le 6$.

how the vortex-splitting of the *unstable* currents, if it occurs, depends on the Reynolds number. To do this, we restrict our attention to the currents with the ratio of Coriolis to inertia forces maintained at $C = 1.0$ and the Reynolds number varied at four additional values of 500, 1000, 2000, and 6000.

Interestingly, for all currents at $C = 1.0$ considered in this study, there are three non-axisymmetric bulges developing along the circumference of the currents irrespective of

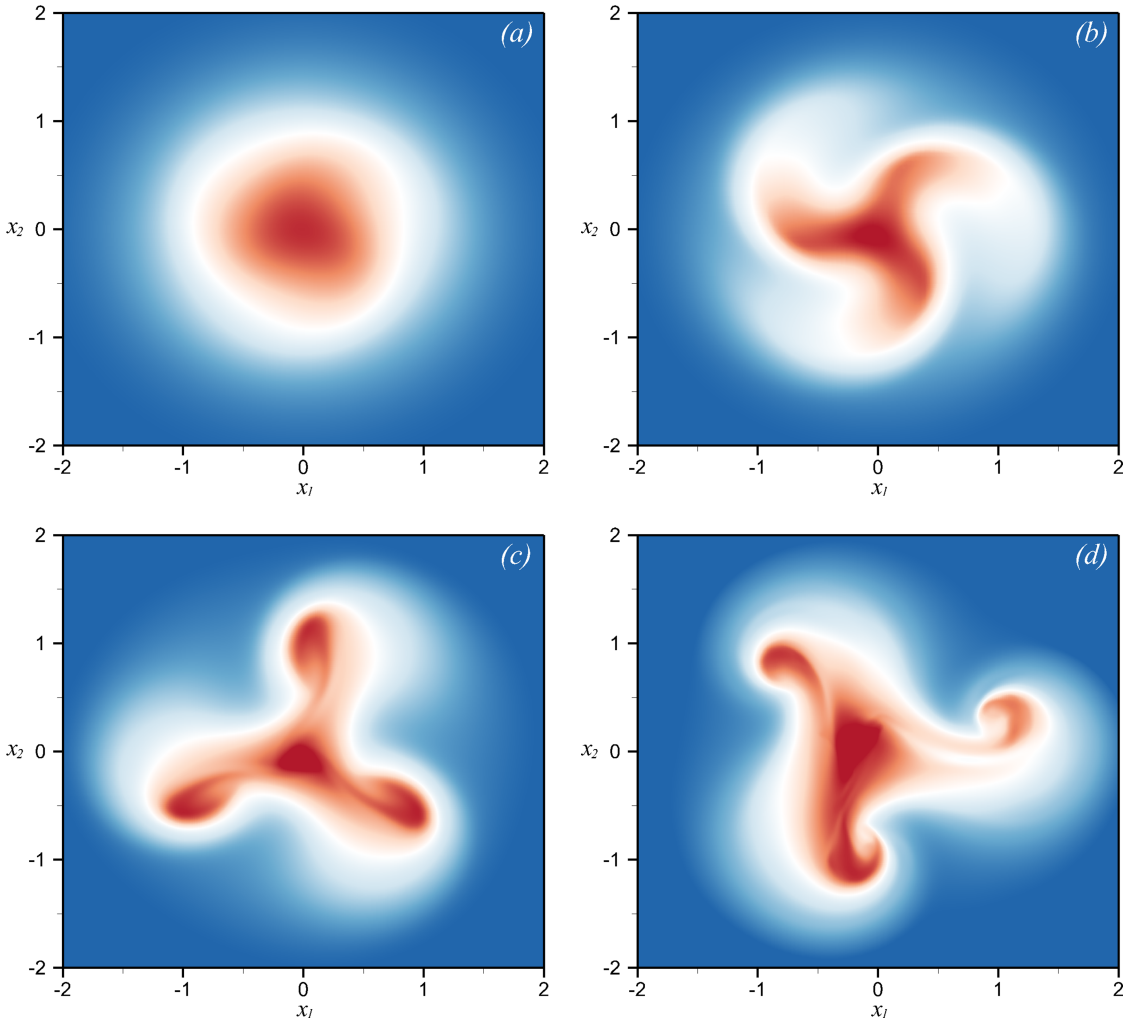

FIG. 12. Rotating cylindrical gravity currents at $C = 1.0$ and different Reynolds numbers, when vortex-splitting begins, visualized by the density averaged in the wall-normal direction, i.e., $\hat{\rho}(x_1, x_2)$, plotted on the (x_1, x_2) plane. For illustrative purposes, the time instances are chosen at $\Omega t/2\pi = 7.5$ for $Re = 500$ (a), $\Omega t/2\pi = 7.1$ for $Re = 1000$ (b), $\Omega t/2\pi = 6.3$ for $Re = 2000$ (c), and $\Omega t/2\pi = 3.5$ for $Re = 6000$ (d).

the Reynolds number. However, depending on the Reynolds number, these non-axisymmetric bulges may or may not grow to an amplitude such that they become cutoff distinct circulations. For the lowest two Reynolds numbers of 500 and 1000 considered in this study, the non-axisymmetric bulges manifest themselves along the circumference of the currents but do not break up into distinct circulations, as shown in Figs. 12(a) and 12(b). For the higher Reynolds numbers considered in this study, i.e., $Re = 2000$ and 6000, it is observed that the non-axisymmetric bulges develop and eventually become cutoff distinct circulations, as shown in Figs. 12(c) and 12(d). Our results indicate that, for the *unstable* currents, the occurrence of vortex-splitting depends not only on the ratio of Coriolis to inertia forces but also on the Reynolds number. Nevertheless, the number of bulges is seen to be independent of the Reynolds number for the range of Reynolds number considered in this study.

IV. CONCLUSIONS

In this study, we investigated the *unstable* cylindrical gravity currents, produced by a full-depth lock release, in a rotating system by means of three-dimensional high-resolution simulations of the incompressible variable-density Navier-Stokes equations with the Coriolis term and using the Boussinesq approximation for small density difference. Here the depth of the fluid is chosen the same as the radius of the cylindrical lock and the ambient fluid is non-stratified. Our attention is focused on the situation when the Coriolis to inertia ratio is larger, namely, $0.5 \leq C \leq 2.0$, in comparison to the parameter range for the *stable* currents investigated in Ref. 28.

Based on the laboratory experiments for the *unstable* currents conducted in Ref. 34, it has been reported that, after the heavy fluid is released from a cylindrical lock, the column of heavy fluid slumps to occupy a conical region and the contraction-relaxation motion diminishes as the quasi-geostrophic equilibrium state is approached. After the quasi-geostrophic equilibrium state, depending on the ratio of Coriolis to inertia forces, different modes of *unstable* currents, i.e., vortex-wandering and vortex-splitting, can be identified. In this study, we confirmed the laboratory observation and revealed more detailed flow information.

Prior to the quasi-geostrophic equilibrium state, the heavy fluid collapses radially outward and a contraction-relaxation

motion is at work for approximately 2–3 revolutions of the system. During the contraction-relaxation motion of the heavy fluid, energy is transformed back and forth between potential energy and kinetic energy, where both show cyclic rise and fall until the quasi-geostrophic equilibrium state is approached. When the contraction-relaxation motion is at work, a new pulse of heavy fluid begins to form near the centre of rotation while the potential energy reaches a local minimum and the kinetic energy reaches a local maximum. As the new pulse moves radially outward, the potential energy increases to a local maximum then decreases to a local minimum, when a new pulse takes form near the centre of rotation.

The quasi-geostrophic equilibrium state is reached after the system has rotated through approximately two to three revolutions. At this transient state of motion, the rate of energy dissipation in the system reaches a local minimum and the potential energy and kinetic energy in the system are maintained at constant levels. The fraction of initial potential energy that is retained in the system, at the quasi-geostrophic equilibrium state, increases as the ratio of Coriolis to inertia forces increases.

After the quasi-geostrophic equilibrium state, depending on the ratio of Coriolis to inertia forces, different modes of *unstable* currents, i.e., vortex-wandering and vortex-splitting, can be observed. When vortex-wandering occurs, i.e., at $C = 0.5$ in this study, the currents move around the centre of rotation in the cyclonic direction without breaking up into multiple vortices. When vortex-splitting occurs, i.e., at $0.75 \leq C \leq 2.0$ in this study, a number of bulges develop along the circumference of the currents and eventually grow to an amplitude such that they become cutoff distinct circulations. A striking feature of the *unstable* currents is the persistent upwelling and downwelling motions for both vortex-wandering and vortex-splitting motions. Although previous numerical investigation on the *unstable* "surface vortex" performed by Ref. 42 identified an entrainment process resulting in dipole-like pairs as in the experiments by Ref. 41, such persistent upwelling and downwelling motions identified here were not reported in previous studies. When vortex-splitting occurs, the kinetic energy in the system increases significantly at the expense of decreasing potential energy. Such an observation confirms that in this study the potential energy is the source for the kinetic energy of non-axisymmetric disturbances via baroclinic instability.

As reasonably expected, the motion of the *unstable* currents depends not only on the ratio of Coriolis to inertia forces but also on the Reynolds number. As we showed, for the *unstable* currents at $C = 1.0$, vortex-splitting occurs for the higher Reynolds number, i.e., $Re = 2000$, 4000, and 6000, considered in this study. On the other hand, for the *unstable* currents at $C = 1.0$, the non-axisymmetric bulges manifest themselves but do not become cutoff distinct circulations for the lower Reynolds numbers, i.e., $Re = 500$ and 1000, considered in this study. Interestingly, the number of bulges, which is a function of the ratio of Coriolis to inertia forces, is seen to be independent of the Reynolds number for the range of Reynolds number considered in this study.

The three-dimensional high-resolution simulations presented in this study complement the existing shallow-water formulation (please see, for example, Refs. 2 and 53). With the use of three-dimensional high-resolution Navier-Stokes simulations, we are now able to provide more detailed flow information that could not be readily obtainable in the shallow-water formulation, e.g., vortex-wandering, vortex-splitting, upwelling and downwelling motions. Furthermore, the simulations provide energy budget analysis which could not be easily attained in the laboratory. Future extensions of the present study may include the partial-depth release cylindrical gravity currents, influence of a stratified ambient[54,55] and non-Boussinesq cases.[27] In these topics, the three-dimensional high-resolution simulations of the type reported here are necessary in further corroboration and progress.

ACKNOWLEDGMENTS

A.D. is grateful for encouragement from Professors P. Linden and S. Dalziel at the University of Cambridge, S. Balachandar at the University of Florida, and M. Garcia and G. Parker at the University of Illinois at Urbana-Champaign. Computational resources are provided by the Computer and Information Networking Center at National Taiwan University. The research is supported by Taiwan Ministry of Science and Technology through Grant Nos. MOST-104-2628-E-002-012-MY3 and MOST-105-2221-E-002-125-MY2.

[1] J. Simpson, *Gravity Currents*, 2nd ed. (Cambridge University Press, 1997).
[2] M. Ungarish, *An Introduction to Gravity Currents and Intrusions* (Chapman & Hall/CRC Press, 2009).
[3] H. E. Huppert and J. Simpson, "The slumping of gravity currents," J. Fluid Mech. **99**, 785–799 (1980).
[4] H. E. Huppert, "The propagation of two-dimensional and axisymmetric viscous gravity currents over a rigid horizontal boundary surface," J. Fluid Mech. **121**, 43–58 (1982).
[5] J. Shin, S. Dalziel, and P. Linden, "Gravity currents produced by lock exchange," J. Fluid Mech. **521**, 1–34 (2004).
[6] B. Marino, L. Thomas, and P. Linden, "The front condition for gravity currents," J. Fluid Mech. **536**, 49–78 (2005).
[7] M. La Rocca, C. Adduce, G. Sciortino, and A. B. Pinzon, "Experimental and numerical simulation of three-dimensional gravity currents on smooth and rough bottom," Phys. Fluids **20**, 106603 (2008).
[8] C. Adduce, G. Sciortino, and S. Proietti, "Gravity currents produced by lock-exchanges: Experiments and simulations with a two layer shallow-water model with entrainment," J. Hydraul. Eng. **138**, 111–121 (2012).
[9] A. Dai, "Experiments on gravity currents propagating on different bottom slopes," J. Fluid Mech. **731**, 117–141 (2013).
[10] A. Dai, "Non-Boussinesq gravity currents propagating on different bottom slopes," J. Fluid Mech. **741**, 658–680 (2014).
[11] V. Lombardi, C. Adduce, G. Sciortino, and M. La Rocca, "Gravity currents flowing upslope: Laboratory experiments and shallow-water simulations," Phys. Fluids **27**, 016602 (2015).
[12] L. Ottolenghi, C. Adduce, R. Inghilesi, V. Armenio, and F. Roman, "Entrainment and mixing in unsteady gravity currents," J. Hydraul. Res. **54**, 541–557 (2016).
[13] L. Ottolenghi, C. Adduce, R. Inghilesi, F. Roman, and V. Armenio, "Mixing in lock-release gravity currents propagating up a slope," Phys. Fluids **28**, 056604 (2016).
[14] C. Härtel, E. Meiburg, and F. Necker, "Analysis and direct numerical simulation of the flow at a gravity-current head. Part 1. Flow topology and front speed for slip and no-slip boundaries," J. Fluid Mech. **418**, 189–212 (2000).
[15] M. Cantero, J. Lee, S. Balachandar, and M. Garcia, "On the front velocity of gravity currents," J. Fluid Mech. **586**, 1–39 (2007).
[16] M. La Rocca, C. Adduce, V. Lombardi, G. Sciortino, and R. Hinkermann, "Development of a lattice Boltzmann method for two-layered shallow-water flow," Int. J. Numer. Methods Fluids **70**, 1048–1072 (2012).

[17]M. La Rocca, C. Adduce, G. Sciortino, P. A. Bateman, and M. A. Boniforti, "A two-layer shallow water model for 3D gravity currents," J. Hydraul. Res. **50**, 208–217 (2012).
[18]A. Dai, "High-resolution simulations of downslope gravity currents in the acceleration phase," Phys. Fluids **27**, 076602 (2015).
[19]A. Dai and Y.-L. Huang, "High-resolution simulations of non-Boussinesq downslope gravity currents in the acceleration phase," Phys. Fluids **28**, 026602 (2016).
[20]R. T. Bonnecaze, M. A. Hallworth, H. E. Huppert, and J. R. Lister, "Axisymmetric particle-driven gravity currents," J. Fluid Mech. **294**, 93–121 (1995).
[21]M. A. Hallworth, H. E. Huppert, J. Phillips, and S. Sparks, "Entrainment into two-dimensional and axisymmetric turbulent gravity currents," J. Fluid Mech. **308**, 289–311 (1996).
[22]M. Ungarish and T. Zemach, "On the slumping of high Reynolds number gravity currents in two-dimensional and axisymmetric configurations," Eur. J. Mech.-B/Fluids **24**, 71–90 (2005).
[23]M. Patterson, J. Simpson, S. Dalziel, and G. Van Heijst, "Vortical motion in the head of an axisymmetric gravity current," Phys. Fluids **18**, 0046601 (2006).
[24]M. Cantero, S. Balachandar, and M. Garcia, "High-resolution simulations of cylindrical density currents," J. Fluid Mech. **590**, 437–469 (2007).
[25]M. Ungarish, "Axisymmetric gravity currents at high Reynolds number–on the quality of shallow-water modeling of experimental observations," Phys. Fluids **19**, 036602 (2007).
[26]M. Ungarish and H. E. Huppert, "Energy balances for axisymmetric gravity currents in homogeneous and linearly stratified ambients," J. Fluid Mech. **616**, 303–326 (2008).
[27]M. Ungarish, "The propagation of high-Reynolds-number non-Boussinesq gravity currents in axisymmetric geometry," J. Fluid Mech. **643**, 267–277 (2010).
[28]A. Dai and C.-S. Wu, "High-resolution simulations of cylindrical gravity currents in a rotating system," J. Fluid Mech. **806**, 71–101 (2016).
[29]R. W. Griffiths, "Gravity currents in rotating systems," Annu. Rev. Fluid Mech. **18**, 59–89 (1986).
[30]R. C. Kloosterziel and G. J. F. Van Heijst, "An experimental study of unstable barotropic vortices in a rotating fluid," J. Fluid Mech. **223**, 1–24 (1991).
[31]A. Mahalov, J. R. Pacheco, S. I. Voropayev, H. J. S. Fernando, and J. C. R. Hunt, "Effects of rotation on fronts of density currents," Phys. Lett. A **270**, 149–156 (2000).
[32]J. R. Pacheco and A. Pacheco-Vega, "Analysis of thin film flows using a flux vector splitting," J. Fluids Eng. **125**, 365–374 (2003).
[33]J. C. R. Hunt, J. R. Pacheco, A. Mahalov, and H. J. S. Fernando, "Effects of rotation and sloping terrain on the fronts of density currents," J. Fluid Mech. **537**, 285–315 (2005).
[34]P. M. Saunders, "The instability of a baroclinic vortex," J. Phys. Oceanogr. **3**, 61–65 (1973).
[35]G. T. Csanady, "The birth and death of a warm core ring," J. Geophys. Res. **84**, 777–780, https://doi.org/10.1029/jc084ic02p00777 (1979).
[36]G. R. Flierl, "A simple model for the structure of warm and cold core rings," J. Geophys. Res. **84**, 781–785, https://doi.org/10.1029/jc084ic02p00781 (1979).
[37]P. D. Killworth, "The time-dependent collapse of a rotating fluid cylinder," J. Phys. Oceanogr. **22**, 390–397 (1992).
[38]M. Ungarish and H. E. Huppert, "The effects of rotation on axisymmetric gravity currents," J. Fluid Mech. **362**, 17–51 (1998).
[39]M. Ungarish and H. E. Huppert, "Simple models of Coriolis-influenced axisymmetric particle-driven gravity currents," Int. J. Multiphase Flow **25**, 715–737 (1999).
[40]M. A. Hallworth, H. E. Huppert, and M. Ungarish, "Axisymmetric gravity currents in a rotating system: Experimental and numerical investigations," J. Fluid Mech. **447**, 1–29 (2001).
[41]R. W. Griffiths and P. F. Linden, "The stability of vortices in a rotating, stratified fluid," J. Fluid Mech. **105**, 283–316 (1981).
[42]R. Verzicco, F. Lalli, and E. Campana, "Dynamics of baroclinic vortices in a rotating, stratified fluid: A numerical study," Phys. Fluids **9**, 419–432 (1997).
[43]F. Necker, C. Härtel, L. Kleiser, and E. Meiburg, "Mixing and dissipation in particle-driven gravity currents," J. Fluid Mech. **545**, 339–372 (2005).
[44]T. Bonometti and S. Balachandar, "Effect of Schmidt number on the structure and propagation of density currents," Theor. Comput. Fluid Dyn. **22**, 341–361 (2008).
[45]M. Cantero, S. Balachandar, M. Garcia, and J. Ferry, "Direct numerical simulations of planar and cylindrical density currents," J. Appl. Mech. **73**, 923–930 (2006).
[46]J. H. Williamson, "Low-storage Runge-Kutta schemes," J. Comput. Phys. **35**, 48–56 (1980).
[47]D. Durran, *Numerical Methods for Wave Equations in Geophysical Fluid Dynamics* (Springer, 1999).
[48]C. Härtel, L. K. M. Michaud, and C. Stein, "A direct numerical simulation approach to the study of intrusion fronts," J. Eng. Math. **32**, 103–120 (1997).
[49]W. K. Dewar and P. D. Killworth, "On the cylinder collapse problem, mixing and the merger of isolated eddies," J. Phys. Oceanogr. **20**, 1563–1575 (1990).
[50]K. B. Winters, P. N. Lombard, J. J. Riley, and E. A. D'Asaro, "Available potential energy and mixing in density-stratified fluids," J. Fluid Mech. **289**, 115–128 (1995).
[51]J. R. Pacheco and R. Verzicco, "Formation of columnar baroclinic vortices in thermally stratified nonlinear spin-up," J. Fluid Mech. **702**, 265–285 (2012).
[52]M. Baghdasarian, A. Pacheco-Vega, and J. R. Pacheco, "Mixing in thermally stratified nonlinear spin-up with uniform boundary fluxes," Phys. Fluids **26**, 096602 (2014).
[53]M. Ungarish, *Hydrodynamics of Suspensions* (Springer-Verlag, 1993).
[54]M. Ungarish and H. E. Huppert, "On gravity currents propagating at the base of a stratified ambient," J. Fluid Mech. **458**, 283–301 (2002).
[55]M. Ungarish, "Gravity currents and intrusions of stratified fluids into a stratified ambient," Environ. Fluid Mech. **12**, 115–132 (2012).